electronic reprint

Acta Crystallographica Section A
**Foundations of Crystallography**
ISSN 0108-7673
Editor: **D. Schwarzenbach**

# Polarization-dependent six-beam X-ray pinhole topographs

**Kouhei Okitsu, Yoshitaka Yoda, Yasuhiko Imai, Yoshinori Ueji, Yuta Urano and XiaoWei Zhang**

Acta Crystallographica Section A
**Foundations of Crystallography**
ISSN 0108-7673

Received 24 February 2006
Accepted 27 April 2006



# Polarization-dependent six-beam X-ray pinhole topographs

**Kouhei Okitsu,[a]* Yoshitaka Yoda,[b] Yasuhiko Imai,[b] Yoshinori Ueji,[c] Yuta Urano[c] and XiaoWei Zhang[d]**

[a]Nano-Engineering Research Center, Institute of Engineering Innovation, Graduate School of Engineering, The University of Tokyo, 2-11-16 Yayoi, Bunkyo-ku, Tokyo 113-8656, Japan, [b]Japan Synchrotron Radiation Research Institute, SPring-8, 1-1-1 Kouto, Mikazuki-cho, Sayo-gun, Hyogo 679-5198, Japan, [c]5-1-5 Kashiwanoha, Kashiwa-shi, Chiba 277-8562, Japan, and [d]Photon Factory, KEK, 1-1 Oho, Tsukuba, Ibaraki 305-0801, Japan. Correspondence e-mail: okitsu@soyak.t.u-tokyo.ac.jp

X-ray six-beam pinhole topograph images were obtained for a silicon crystal with incident synchrotron X-rays. The polarization state of X-rays incident on the sample crystal was controlled by using a four-quadrant phase-retarder system [Okitsu *et al.* (2002). *Acta Cryst.* A**58**, 146–154] that can be rotated around the transmitted beam axis to generate arbitrarily polarized X-rays. Quantitative agreement was found between the experimental and computer-simulated topograph images based on the *n*-beam Takagi–Taupin dynamical theory under the assumption that the polarization state of the incident X-rays was identical with the experiment. This result confirmed the validity of the computer algorithm to solve the *n*-beam dynamical theory and the proper operation of the rotating four-quadrant phase-retarder system simultaneously.

## 1. Introduction

In the history of development of X-ray dynamical diffraction theories, the Takagi–Taupin equation (Takagi, 1962, 1969; Taupin, 1964) is worthy of special mention since it can deal with the behavior of X-rays in a distorted crystal while the previous X-ray two-beam dynamical theories (Darwin, 1914*a*,*b*; Ewald, 1917; von Laue, 1931) can only deal with X-ray wavefields in a perfect crystal.

On the other hand, extensions of the Ewald–Laue dynamical theory (Ewald, 1917; von Laue, 1931) to *n*-beam cases were published by Hildebrandt (1967), Ewald & Héno (1968) and Héno & Ewald (1968). A numerical method to solve the theory was given by Colella (1974). This work stimulated many authors to develop the three-beam method for solving the phase problem in crystal structure analysis which were reviewed by Colella (1995*a*,*b*), Weckert & Hümmer (1997, 1998) and Chang (1998, 2004).

Okitsu (2003) has generalized the Takagi–Taupin equation to *n*-beam cases ($n \in \{3, 4, 6, 8, 12\}$) taking into account the polarization effect. Before this work, Thorkildsen presented an extended form of the Takagi–Taupin equation to the three-beam case (Thorkildsen, 1987; Thorkildsen & Larsen, 1998) neglecting the polarization effect. Further, Larsen & Thorkildsen (1998) considered the polarization effect on the analytical solution of the three-beam Takagi–Taupin equation. However, this consideration was limited to a geometry that the authors referred to as 'symmetrical scattering'. In Chang's book (Chang, 2004), the equation that is equivalent to equation (25) of Okitsu (2003) appears as equation (7.354). However, this equation does not have a lattice-displacement term. The present authors (Okitsu *et al.*, 2003) have shown a qualitative agreement between six-beam pinhole topograph images experimentally obtained and computer-simulated using an algorithm based on the theory (Okitsu, 2003). In the present paper, more generalized forms of the equations than those described in Okitsu (2003) are presented first, and these are followed by some considerations of the equations. Then, six-beam pinhole topographs experimentally obtained and computer simulated using the generalized equation are presented. They verify the *n*-beam Takagi–Taupin equation more clearly than in the previous paper (Okitsu *et al.*, 2003). In particular, dependence of the polarization state of the incident X-rays on the excited wavefield in the crystal is clarified.

A comparison between experimental and computer-simulated *n*-beam ($n = 3$) pinhole topographs was published by Heyroth *et al.* (2001) for the first time. The authors of this work obtained the computer-simulated images by superposing coherently plane wave solutions of the *n*-beam ($n = 3$) dynamical theory (Hildebrandt, 1967; Ewald & Héno, 1968; Héno & Ewald, 1968; Colella, 1974). The present work gives another method to simulate numerically *n*-beam ($n = 6$) pinhole topographs.

## 2. Theory

Takagi's fundamental equation of the dynamical theory which appeared as equation (30) in Takagi (1969) can be

transformed with a procedure described using equations (9)–(15) in Okitsu (2003) as follows:

$$(\mathbf{s}_i \cdot \mathrm{grad})\mathbf{D}_i(\mathbf{r}) = -\mathrm{i}\pi K \sum_{j\neq i} \chi_{h_i-h_j} \exp[\mathrm{i}2\pi(\mathbf{h}_i - \mathbf{h}_j)\cdot\mathbf{u}(\mathbf{r})][\mathbf{D}_j(\mathbf{r})]_{\mathbf{s}_i}.$$

Here, $\mathbf{s}_i$ is a unit vector in the direction of propagation of the $i$th-numbered wave, $\mathbf{D}_i(\mathbf{r})$ is a complex amplitude vector of the $i$th-numbered wave at position $\mathbf{r}$ in the crystal, $K$ is the wavenumber of X-rays in vacuum, $\mathbf{h}_i$ and $\mathbf{h}_j$ are reflection vectors giving $i$th- and $j$th-order reflected X-ray beams, $\chi_{h_i-h_j}$ is the $(\mathbf{h}_i - \mathbf{h}_j)$-order Fourier coefficient of electric susceptibility, $\mathbf{u}(\mathbf{r})$ is the lattice displacement vector and $[\mathbf{D}_j(\mathbf{r})]_{\mathbf{s}_i}$ is a component vector of $\mathbf{D}_j(\mathbf{r})$ which is perpendicular to $\mathbf{s}_i$. With an approximation that intensities of excited X-ray beams other than $n$ beams are negligible, the whole wavefield $\mathbf{D}$ is described as follows:

$$\mathbf{D} = \sum_{i=0}^{n-1} \mathbf{D}_i(\mathbf{r}) \exp\left(-\mathrm{i}2\pi\overrightarrow{\mathrm{Lo}H_i}\cdot\mathbf{r}\right). \quad (1)$$

Here, Lo is the Lorenz point and $H_i$ is the $i$th reciprocal-lattice node.

In Okitsu (2003), $\mathbf{D}_i(\mathbf{r})$ was represented as a linear combination of $\mathbf{e}_i$ and $\mathbf{e}_{(i+1)'}$. Here, $\mathbf{e}_i$ is defined by $\mathbf{e}_i = (\mathbf{s}_{(i-1)'} \times \mathbf{s}_i)/|\mathbf{s}_{(i-1)'} \times \mathbf{s}_i|$, where $(i+1)'$ and $(i-1)'$ are mod $[(i+1), n]$ and mod $[(i-1), n]$, respectively [see Fig. 5 of Okitsu (2003)]. However, this representation is not necessary. In general, $\mathbf{D}_k(\mathbf{r})$ $(k \in \{i, j\})$ can be written as

$$\mathbf{D}_k(\mathbf{r}) = D_k^{(0)}(\mathbf{r})\mathbf{e}_k^{(0)} + D_k^{(1)}(\mathbf{r})\mathbf{e}_k^{(1)}, \quad k \in \{i, j\}.$$

Here, $\mathbf{e}_k^{(0)}$ and $\mathbf{e}_k^{(1)}$ are a couple of unit vectors. These vectors should be perpendicular to $\mathbf{s}_i$ and may cross orthogonally or obliquely with each other, in general. However, for convenience in the following description, let us set $\mathbf{e}_k^{(0)}$ and $\mathbf{e}_k^{(1)}$, referring to Fig. 1 of Okitsu (2003), as

$$\mathbf{e}_k^{(0)} = \frac{\mathbf{s}_k \times \overrightarrow{PQ}}{\left|\mathbf{s}_k \times \overrightarrow{PQ}\right|},$$
$$\mathbf{e}_k^{(1)} = \mathbf{s}_k \times \mathbf{e}_k^{(0)}.$$

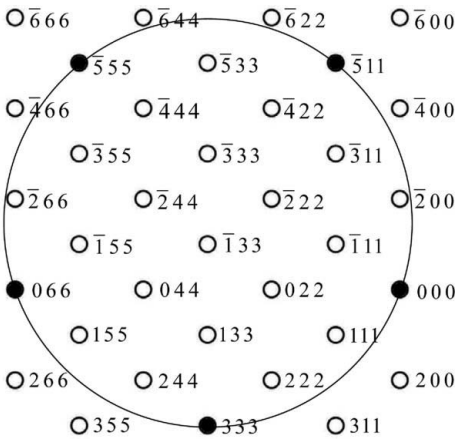


**Figure 1**
Illustration of the five lattice nodes in reciprocal space chosen to build a five-beam case in silicon.

Here, $P$ is the starting point of the wavevector of the incident X-rays and $Q$ is the center of the circle on which the $n$ reciprocal-lattice nodes are situated. Now, let us define the polarization factors $S$ and $C$ as follows:

$$\mathbf{e}_j^{(m)} = S_{i,j}^{(m)}\mathbf{s}_i + C_{i,j}^{(0,m)}\mathbf{e}_i^{(0)} + C_{i,j}^{(1,m)}\mathbf{e}_i^{(1)}. \quad (2)$$

By using a procedure similar to that used when deriving equation (25) from equation (15) in Okitsu (2003), the following equation can be obtained:

$$\frac{\partial}{\partial s_i} D_i^{(l)}(\mathbf{r}) = -\mathrm{i}\pi K \sum_{j\neq i} \sum_{m=0}^{1} \{\chi_{h_i-h_j} \exp[\mathrm{i}2\pi(\mathbf{h}_i - \mathbf{h}_j)\cdot\mathbf{u}(\mathbf{r})] \times C_{i,j}^{(l,m)} D_j^{(m)}(\mathbf{r})\}, \quad (3)$$

where $i, j \in \{0, 1, \ldots, n-1\}$, $l, m \in \{0, 1\}$, $n \in \{2, 3, 4, 5, 6, 8, 12\}$.

Here, $i$ and $j$ are ordinal numbers of waves and $l$ and $m$ indicate the polarization states of the X-rays. $D_i^{(l)}(\mathbf{r})$ and $D_j^{(m)}(\mathbf{r})$ are scalar amplitudes modulating the waves written as $\mathbf{e}_i^{(l)} \exp(-\mathrm{i}2\pi\overrightarrow{\mathrm{Lo}H_i}\cdot\mathbf{r})$ and $\mathbf{e}_j^{(m)} \exp(-\mathrm{i}2\pi\overrightarrow{\mathrm{Lo}H_j}\cdot\mathbf{r})$. The value of $n$ was restricted to $n \in \{3, 4, 6, 8, 12\}$ in Okitsu (2003). However, cases of $n = 2$ and $n = 5$ should be added. $n = 2$ does not have to be dealt with as an exception owing to the generalized definition of polarization factors by equation (2). Cases of $n = 5$ should be allowed for the diamond structure, *e.g.* see Fig. 1. The restriction that $n \in \{2, 3, 4, 5, 6, 8, 12\}$ is based on the fact that $n$ reciprocal-lattice nodes should be situated on a circle in reciprocal space. This is a necessary restriction, not just for convenience in describing the geometrical situation. Figs. 3 and 4 of Okitsu (2003) show four-beam cases to be dealt with by equations (3) or (4) as $n = 4$ and to be dealt with as incoherent superposition of four three-beam cases, respectively. In both Figs. 3 and 4 of Okitsu (2003), four reciprocal-lattice nodes are on an Ewald sphere. However, only the former case can be dealt with by (3) or (4) as $n = 4$. This is because finite angular divergence and energy spread of the incident X-rays should always be taken into account when describing a practical condition of experiment. Whether $n$ reciprocal-lattice nodes are situated on a circle or not is a critical factor for practical calculation using (3) or (4).

Here, let us discuss the relation between the Lorentz point Lo and the Laue point La. $\overrightarrow{\mathrm{LaLo}}$ $(= \overrightarrow{\mathrm{La}H_i} - \overrightarrow{\mathrm{Lo}H_i})$ has real and imaginary components $\overrightarrow{\mathrm{LaLo}^{(R)}}$ and $\overrightarrow{\mathrm{LaLo}^{(I)}}$, *i.e.* $\overrightarrow{\mathrm{LaLo}} = \overrightarrow{\mathrm{LaLo}^{(R)}} + \mathrm{i}\overrightarrow{\mathrm{LaLo}^{(I)}}$. As considered by Härtwig (1987), there is an ambiguity about the direction of $\overrightarrow{\mathrm{LaLo}^{(I)}}$. Härtwig (1987) concluded that only $\overrightarrow{\mathrm{LaLo}^{(I)}}$ which is parallel to $\overrightarrow{n}$ has concrete physical meaning. Here, $\overrightarrow{n}$ is the downward normal of the entrance surface of the crystal. However, this restriction disables the solution of (3) when the entrance surface of the crystal is not planar. This difficulty can be completely avoided by using (4) below.

The right-hand side of (3) has a summation $\sum_{j\neq i}$ and then does not have a term containing $\chi_0$ explicitly. However, the term $\chi_0$ can be used not only for mathematical convenience but also for physical importance. The following equation is

obtained by using the same procedure as that used when deriving equation (39) from equation (25) in Okitsu (2003):

$$\frac{\partial}{\partial s_i} D_i^{\prime(l)}(\mathbf{r}) = -\mathrm{i}\pi K \sum_{j=0}^{n-1} \sum_{m=0}^{1} \{\chi_{h_i-h_j} \exp[\mathrm{i}2\pi(\mathbf{h}_i - \mathbf{h}_j)\cdot\mathbf{u}(\mathbf{r})] \times C_{i,j}^{(l,m)} D_j^{\prime(m)}(\mathbf{r})\}, \quad (4)$$

where $i, j \in \{0, 1, \ldots, n-1\}$, $l, m \in \{0, 1\}$, $n \in \{2, 3, 4, 5, 6, 8, 12\}$.

Here, $D_i^{\prime(l)}(\mathbf{r})$ and $D_j^{\prime(m)}(\mathbf{r})$ are scalar amplitudes modulating the waves written as $\mathbf{e}_i^{(l)} \exp(-\mathrm{i}2\pi\overrightarrow{\mathrm{La}H_i}\cdot\mathbf{r})$ and $\mathbf{e}_j^{(m)} \exp(-\mathrm{i}2\pi\overrightarrow{\mathrm{La}H_j}\cdot\mathbf{r})$. Equation (4) enables a computer simulation under a situation that the Laue and Bragg cases coexist in $n$-beam cases and the crystal has an arbitrary shape by assuming that $\chi_{\mathbf{h}_i-\mathbf{h}_j}(\mathbf{r}_v) = 0$ for all cases of $i, j \in \{0, 1, \ldots, n-1\}$, where $\mathbf{r}_v$ is in vacuum.

Incidentally, a description of so-called Renninger scans (Renninger, 1937) can be found in §9.2.1 of Authier's (2005) book. This is one of the important techniques of goniometry to survey the $n$-beam X-ray diffraction. While the present paper is focused on $n$-beam topography but not on goniometry, an equation that has terms of angular deviation of the incident X-rays explicitly can easily be derived. Let us define $\overrightarrow{P_1H_0}$ as a wavevector of the incident X-rays which is angularly deviated by $-\overrightarrow{P_1\mathrm{La}}$ from the Laue point La. Suppose that the sphere surface whose center and radius are $H_0$ and $K$ can approximately be regarded as a flat plane in the vicinity of the Laue point La, then $\overrightarrow{P_1\mathrm{La}}$ can be written as

$$\overrightarrow{P_1\mathrm{La}} = K(\beta^{(0)}\mathbf{e}_0^{(0)} + \beta^{(1)}\mathbf{e}_0^{(1)}). \quad (5)$$

Here, $\beta^{(0)}$ and $\beta^{(1)}$ are angular deviations of the incident X-rays from the strict $n$-beam condition. Let us define a unitary transform as

$$D_k^{\prime(l)}(\mathbf{r}) = D_k^{\prime\prime(l)}(\mathbf{r}) \exp(-\mathrm{i}2\pi\overrightarrow{P_1\mathrm{La}}\cdot\mathbf{r}), \quad k \in \{i, j\}. \quad (6)$$

By substituting (5) and (6) into (4), the following equation can be obtained:

$$\frac{\partial}{\partial s_i} D_i^{\prime\prime(l)}(\mathbf{r}) = \mathrm{i}2\pi K(\beta^{(0)}S_{i,0}^{(0)} + \beta^{(1)}S_{i,0}^{(1)})D_i^{\prime\prime(l)}(\mathbf{r}) - \mathrm{i}\pi K \sum_{j=0}^{n-1} \sum_{m=0}^{1} \{\chi_{h_i-h_j} \exp[\mathrm{i}2\pi(\mathbf{h}_i - \mathbf{h}_j)\cdot\mathbf{u}(\mathbf{r})] \times C_{i,j}^{(l,m)} D_j^{\prime\prime(m)}(\mathbf{r})\}, \quad (7)$$

where $i, j \in \{0, 1, \ldots, n-1\}$, $l, m \in \{0, 1\}$, $n \in \{2, 3, 4, 5, 6, 8, 12\}$.

Here, $D_k^{\prime\prime(l)}(\mathbf{r})$ ($k \in \{i, j\}$) are scalar amplitudes modulating the waves written as $\mathbf{e}_k^{(l)} \exp(-\mathrm{i}2\pi\overrightarrow{P_1H_i}\cdot\mathbf{r})$.

## 3. Computer simulation

In the present study, the following equation was used to calculate the X-ray wavefield in the crystal in place of equation (40) of Okitsu (2003):

$$\frac{D_i^{\prime(l)}(R^{(1)}) - D_i^{\prime(l)}(R_i^{(0)})}{\left|\overrightarrow{R_i^{(0)}R^{(1)}}\right|} = -\mathrm{i}\pi K \sum_{j=0}^{n-1} \sum_{m=0}^{1} \left\{ \chi_{h_i-h_j} \exp[\mathrm{i}2\pi(\mathbf{h}_i - \mathbf{h}_j)\cdot\mathbf{u}(Rm_i)] \times C_{i,j}^{(l,m)} \frac{D_j^{\prime(m)}(R_i^{(0)}) + D_j^{\prime(m)}(R^{(1)})}{2} \right\}. \quad (8)$$

Here, $D_i^{\prime(l)}(R_i^{(0)})$ and $D_i^{\prime(l)}(R^{(1)})$ are complex amplitudes of X-rays whose polarization state is $l$ at positions $R_i^{(0)}$ and $R^{(1)}$. $\mathbf{u}(Rm_i)$ is the lattice displacement vector at $Rm_i$ which was assumed to be a zero vector in the present case. The simultaneous linear equation (8) can be solved by using a $12 \times 12$ ($2n \times 2n$) matrix calculation. The method to solve (8) numerically is fundamentally the same as that described in §3 of Okitsu (2003). To obtain a solution of (8) in a six-beam case, the crystal has to be divided into hexagonal pyramids, as shown in Fig. 2(*a*), small enough compared to the extinction distance of forward diffraction $-1/\chi_0 K$. $-1/\chi_0 K$ was calculated to be 23.36 µm in the present case (a photon energy of 18.245 keV). The height of the small pyramid is Th/2000, where Th (= 9.6 mm) is the thickness of the sample crystal. $\left|\overrightarrow{R_i^{(0)}R^{(1)}}\right|$ in Fig. 2(*a*) is calculated to be 6.795 µm, which is small enough compared with $-1/\chi_0 K$. Then the calculation

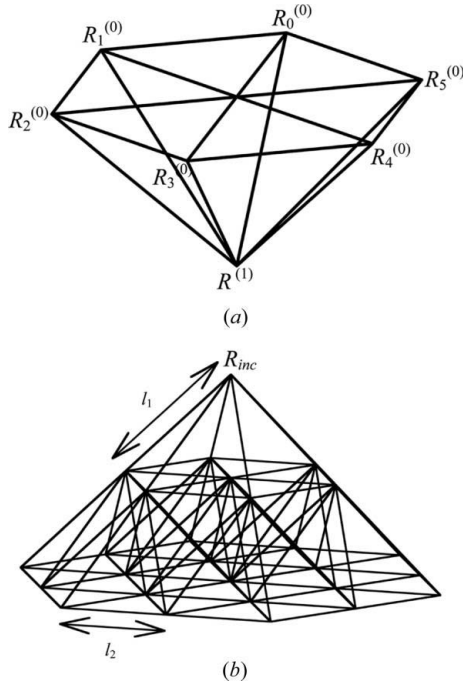


**Figure 2**
(*a*) The crystal has to be three-dimensionally divided into sufficiently small wedges to solve equation (8). This is a six-beam case. (*b*) is a reproduction of Fig. 3 in Okitsu *et al.* (2003). For a boundary condition to solve equation (8) in the case of pinhole topography, amplitude values $D_0^{(0)}(R_{\mathrm{inc}})$ and/or $D_0^{(1)}(R_{\mathrm{inc}})$, depending on the polarization state of the incident X-rays, have to be given only at the incidence point of X-rays $R_{\mathrm{inc}}$ on the entrance surface of the crystal. $l_1$ and $l_2$ were calculated to be 6.795 and 4.809 µm.

**Table 1**
Parameters of X-ray reflection indices of a silicon crystal: $\theta_B$ is the Bragg reflection angle; $|F_{\mathbf{h}}|$ is the absolute value of the crystal structure factor; $|\chi_{\mathbf{h}r}|$ and $|\chi_{\mathbf{h}i}|$ are the absolute values of real and imaginary parts of $\chi_{\mathbf{h}}$.

Here, $\chi_{\mathbf{h}}$ is the **h**th-order Fourier coefficient of electric susceptibility of the silicon crystal.

| **h** | $2\theta_B$ (°) | $\lvert F_{\mathbf{h}}\rvert$ | $\lvert\chi_{\mathbf{h}r}\rvert \times 10^{-6}$ | $\lvert\chi_{\mathbf{h}i}\rvert \times 10^{-7}$ |
|---|---|---|---|---|
| 0 0 0 | 0.0000 | 112.5153 | 2.9092 | 0.1334 |
| 4 4 0 | 41.4510 | 43.176 | 1.1163 | 0.1179 |
| 4 8 4 | 75.6074 | 17.690 | 0.4573 | 0.0921 |
| 0 8 8 | 90.1096 | 12.671 | 0.3275 | 0.0813 |
| $\bar{4}$ 4 8 | 75.6074 | 17.690 | 0.4573 | 0.0921 |
| $\bar{4}$ 0 4 | 41.4510 | 43.176 | 1.1163 | 0.1179 |

was performed layer by layer with a thickness of 4.8 μm (= Th/2000) by solving (8) at $Rm_i$ [see Fig. 2(*a*)].

For a boundary condition to solve (8) in the case of pinhole topography, only at the incidence point of X-rays $R_{\rm inc}$ [see Fig. 2(*b*)] on the entrance surface of the crystal do non-zero values of X-ray amplitudes have to be given for $D_0^{(0)}(R_{\rm inc})$ and $D_0^{(1)}(R_{\rm inc})$, which depend on the polarization state of the incident X-rays. Only on the surfaces of and inside the hexagonal pyramid drawn in Fig. 2(*b*) can a non-zero solution be obtained. Let us define $D_i^{(l)}(D_0^{(0)}(R_{\rm inc}), D_0^{(1)}(R_{\rm inc}), R_{\rm exit})$ ($i \in \{0, 1, 2, 3, 4, 5\}$, $l \in \{0, 1\}$) as solutions of (8) obtained at $R_{\rm exit}$, a position on the exit surface of the crystal with boundary condition $D_0^{(0)}(R_{\rm inc})$ and $D_0^{(1)}(R_{\rm inc})$. A general solution with an incidence of arbitrarily polarized X-rays can be calculated from a linear combination of $D_i^{(l)}(1, 0, R_{\rm exit})$ and $D_i^{(l)}(0, 1, R_{\rm exit})$. For example, a solution with an incidence of left-screwed circular polarization can be calculated to be

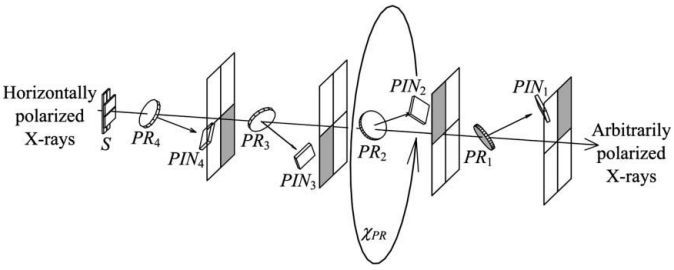


**Figure 3**
A four-quadrant X-ray phase-retarder system (Okitsu *et al.*, 2002) which consists of four [100]-oriented diamond transmission-type phase retarders (Hirano *et al.*, 1991, 1992, 1993; Giles, Malgrange, Goulon, de Bergevin, Vettier, Dartyge *et al.*, 1994; Giles, Malgrange, Goulon, de Bergevin, Vettier, Fontaine *et al.*, 1994; Suzuki *et al.*, 1998). $PR_1$, $PR_2$, $PR_3$ and $PR_4$ give 111 Laue-case (see Fig. 4) reflection in the first-, second-, third- and fourth-quadrant directions viewed from the downstream direction, *i.e.* the planes of incidence are inclined from the horizontal plane by 45, 135, 225 and 315° when $\chi_{PR} = 0$. $\chi_{PR}$ is a rotation angle of the $\chi$-circle goniometer which is equipped with the whole phase-retarder system. $\chi_{PR}$ can be controlled in a range of ±45° to generate arbitrarily polarized X-rays with a high degree of polarization. This is due to the compensation effect for the off-axis and chromatic aberrations and is also due to the total effective thickness (= 7.941 mm) achieved by using four diamond crystals. The rocking curves of the four diamond crystals were monitored with four PIN photo diodes. The beam dimension was limited by a four-quadrant slit *S* placed upstream of the whole system.

$[D_i^{(l)}(1, 0, R_{\rm exit}) - {\rm i}D_i^{(l)}(0, 1, R_{\rm exit})]/2^{1/2}$. Reflection parameters of the silicon crystal used when performing the simulation are summarized in Table 1. Each calculation for obtaining $D_i^{(l)}(1, 0, R_{\rm exit})$ and $D_i^{(l)}(0, 1, R_{\rm exit})$ took three weeks of CPU time on a personal computer with a Pentium III 1 GHz processor. Tones of all computer-simulated images with a pixel size of 10.05 × 10.05 μm were tuned with an identical tone curve by using Adobe Photoshop 7.0. Both experimental and computer-simulated pinhole topographs shown in Figs. 8–14 are negative images.

## 4. Experimental

### 4.1. Phase-retarder system

The experiments were performed using the first-order undulator beam at BL09XU of SPring-8. The synchrotron X-rays were monochromated to 18.245 keV (a wavelength of 0.6795 Å) with a water-cooled silicon monochromator system giving a twice-bounced 111 reflection. Fig. 3 shows a schematic drawing of a four-quadrant X-ray phase-retarder system (Okitsu *et al.*, 2002) mounted on a $\chi$-circle-type goniometer. The position and direction of the rotation axis $\chi_{PR}$ in Fig. 3 were adjusted to be identical with the transmitted X-ray beam axis. The phase retarders were [100]-oriented parallel-sided and approximately round diamond crystals with diameters of about 3 mm, which were synthesized by Sumitomo Electric Industries, Ltd. All of them were used in the vicinity of the arrangement shown in Fig. 4 giving 111 reflection in an asymmetric Laue geometry. The thicknesses of the phase-retarder crystals $PR_1$, $PR_2$, $PR_3$ and $PR_4$ in Fig. 3 were 1.545, 2.198, 1.565 and 2.633 mm. The total thickness was 7.941 mm, which cannot be achieved by a single diamond crystal. The diamond crystals were mounted on tangential-bar-type goniometers so that $[0\bar{1}1]$ axes were parallel to the axes of the goniometers. 35.38% of the incident X-rays was transmitted through the four diamond crystals.

The degree of vertical polarization generated with the phase-retarder system was estimated using the polarization analyzer shown in Fig. 5. The analyzer was made of a monolithic silicon channel-cut crystal equipped with a Hart–Rodrigues offset mechanism (Hart & Rodrigues, 1979) giving 955 twice-bounced reflection in an asymmetric Bragg geometry as shown in Fig. 5. An angular offset was applied to

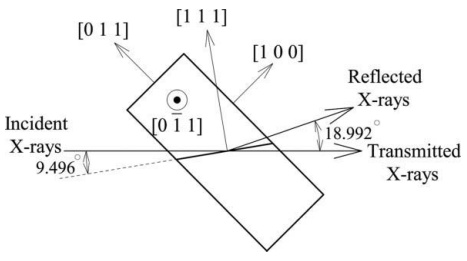


**Figure 4**
All of the four diamond phase retarders were used in the vicinity of this arrangement giving 111 reflection in an asymmetric Laue geometry.

the channel of the analyzer so that the reflectivity was reduced to half the value of the maximum. Owing to this offset mechanism in addition to the Bragg angle nearly equal to 45° (45.73° at 18.245 keV), a high value of $\sigma$–$\pi$ reflectivity ratio ($>10^4$) was achieved. Fig. 6 shows the ratio of the horizontally polarized component to the total X-ray intensity (logarithmic scale plotted on the left ordinate) together with the rocking curve of $PR_1$ (the right ordinate). Before performing the measurement shown in Fig. 6, the $\chi_{PR}$ circle of the phase-retarder system was adjusted so that the planes of incidence of $PR_1$, $PR_2$, $PR_3$ and $PR_4$ were inclined by 45, 135, 225 and 315° from the horizontal plane viewed from the downstream direction. Angular deviations $\Delta\theta_{PR_n}$ ($n \in \{1, 2, 3, 4\}$; only in the present subsection is symbol $n$ used for denoting the quadrant number of phase retarders) of the $n$-numbered-quadrant phase retarder $PR_n$ from the Bragg condition were controlled during the measurement so that the absolute values of phase-shift gradient grad$[\Delta\phi_n(\Delta\mathbf{k})]$ have identical values for $n \in \{1, 2, 3, 4\}$ in reciprocal space (Okitsu *et al.*, 2002). Here, $\Delta\phi_n(\Delta\mathbf{k})$ is a $\sigma$–$\pi$ phase shift given by the $n$-numbered-quadrant phase retarder at a position $\Delta\mathbf{k}$, which is the deviation of the wavevector of the incident X-rays from the Bragg condition in reciprocal space. According to Hirano *et al.* (1995), a $\sigma$–$\pi$ phase shift given by a transmission-type single phase retarder $\Delta\phi(\Delta\theta_{PR})$ is approximately given by

$$\Delta\phi(\Delta\theta_{PR}) \approx \frac{cz}{\Delta\theta_{PR}},$$

where $c$ is a constant depending on the photon energy and the geometrical condition of the phase retarder, and $z$ is the thickness of the phase retarder. $\Delta\theta_{PR}$ is an angular deviation from the Bragg condition of the phase retarder. Therefore,

$$\begin{aligned}\text{grad}[\Delta\phi_n(\Delta\mathbf{k})] &\propto \frac{\mathrm{d}}{\mathrm{d}\Delta\theta_{PR_n}}\Delta\phi_n(\Delta\theta_{PR_n}) \\ &\propto -\frac{cz_n}{|\Delta\theta_{PR_n}|^2},\end{aligned}$$

where $z_n$ is the thickness of the $n$-numbered-quadrant phase retarder $PR_n$. In order to optimize the effect of compensation for the off-axis and chromatic aberrations, $\Delta\theta_{PR_n}$ were controlled during the angular scan shown in Fig. 6 so as to keep the following condition:

$$\frac{z_1}{|\Delta\theta_{PR_1}|^2} = \frac{z_2}{|\Delta\theta_{PR_2}|^2} = \frac{z_3}{|\Delta\theta_{PR_3}|^2} = \frac{z_4}{|\Delta\theta_{PR_4}|^2}. \quad (9)$$

The total phase shift $\Delta\phi_{\text{total}}$ is given by

$$\Delta\phi_{\text{total}} = -\frac{cz_1}{\Delta\theta_{PR_1}} + \frac{cz_2}{\Delta\theta_{PR_2}} - \frac{cz_3}{\Delta\theta_{PR_3}} + \frac{cz_4}{\Delta\theta_{PR_4}}. \quad (10)$$

The reversal of the sign of the phase shift given by the even- and odd-numbered-quadrant phase retarders is due to the reversal of the directions of $\sigma$ and $\pi$ polarizations. With the arrangement shown in Fig. 5 placed downstream of the phase-retarder system shown in Fig. 3, the number of photons was counted for 1 s at each angular position of the phase retarders. The measurement was performed with a scintillation counter behind the polarization analyzer fixed at an angular position giving the maximum reflectivity, rotating step by step the four diamond crystals simultaneously so as to satisfy the condition given by equation (9). The signs of $\Delta\theta_{PR_n}$ were controlled to be opposite for the odd- and even-numbered-quadrant phase retarders. The scan step of $\Delta\theta_{PR_1}$ was changed with respect to the scan range as summarized in Table 2. Since the monochromated undulator beam was too strong, an aluminium absorber with a thickness of 2.3 mm was inserted just behind the slit $S$ in Fig. 3 whose aperture was 100 × 100 µm. The value plotted on the left ordinate in Fig. 6 was normalized with

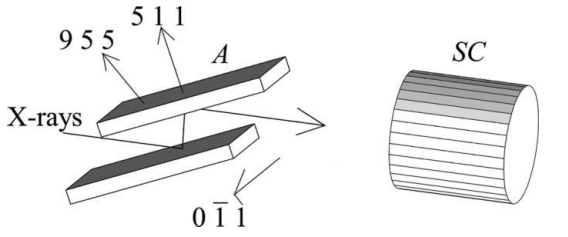


**Figure 5**
A polarization analyzer ($A$) made of a monolithic channel-cut silicon crystal equipped with a Hart–Rodrigues offset mechanism (Hart & Rodrigues, 1979). Only the horizontally polarized component of the incident X-rays was counted with an NaI scintillation counter (SC). A high $\sigma$–$\pi$ reflectivity ratio ($>10^4$) can be achieved owing to the angular offset applied to the channel in addition to the Bragg angle nearly equal to 45° (45.73° at 18.245 keV) for the 955 reflection.

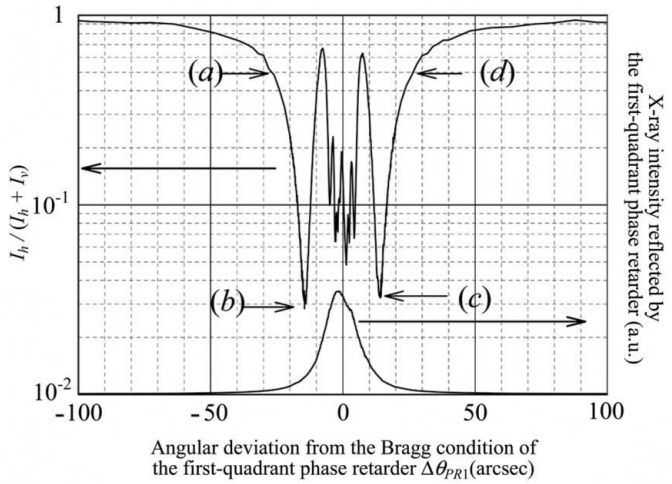


**Figure 6**
$I_h(\Delta\theta_{PR_1})/[I_h(\Delta\theta_{PR_1}) + I_v(\Delta\theta_{PR_1})]$ is plotted on a logarithmic scale (the left ordinate), where $I_h$ and $I_v$ are intensity components of horizontally and vertically polarized X-rays. $I_h$ was directly counted with a scintillation counter (SC in Fig. 5). $[I_h(\Delta\theta_{PR_1}) + I_v(\Delta\theta_{PR_1})]$ was estimated to be 8500 counts s$^{-1}$ from $I_h(-400\,\text{arcsec}) = 8500$ counts s$^{-1}$, where $I_v$ was sufficiently small compared with $I_h$. ($a$) and ($d$) are angular positions of $\Delta\theta_{PR_1} = -27.52, +27.08$ arcsec, where right- and left-screwed circularly polarized X-rays are generated. ($b$) and ($c$) are positions of $\Delta\theta_{PR_1} = -14.80, +14.08$ arcsec, where vertically polarized X-rays are generated. The profile having a maximum in the vicinity of $\Delta\theta_{PR_1} = 0$ is a rocking curve of X-rays reflected by the first-quadrant phase retarder $PR_1$ monitored with a photodiode $\text{PIN}_1$ in Fig. 3 (the right ordinate on a linear scale).

**Table 2**
The experimental result shown in Fig. 6 was obtained under the following conditions: $|\Delta\theta_{PR_1}|^{(\mathrm{Max})}$ and $|\Delta\theta_{PR_1}|^{(\mathrm{Min})}$: maximum and minimum absolute values of measured ranges of $\Delta\theta_{PR_1}$, where $\Delta\theta_{PR_1}$ is the angular deviation from the Bragg condition of the first-quadrant phase retarder in arcsec, $\Delta\theta_{PR_1}^{(\mathrm{Step})}$: angular step in arcsec; measuring time was 1 s at every measuring point.

| | $\lvert\Delta\theta_{PR_1}\rvert^{(\mathrm{Max})}$ (arcsec) | $\lvert\Delta\theta_{PR_1}\rvert^{(\mathrm{Min})}$ (arcsec) | $\Delta\theta_{PR_1}^{(\mathrm{Step})}$ (arcsec) |
|---|---|---|---|
| Range 1 | 400.00 | 240.00 | 40.00 |
| Range 2 | 240.00 | 40.00 | 8.00 |
| Range 3 | 40.00 | 20.00 | 2.00 |
| Range 4 | 20.00 | 15.20 | 0.08 |
| Range 5 | 15.20 | 14.40 | 0.04 |
| Range 6 | 14.40 | 0.00 | 0.16 |

the number of photons (8500 counts $s^{-1}$) counted at $\Delta\theta_{PR} = \pm 400$ arcsec keeping the condition of (9).

The degree of vertical polarization $P_v$ is defined by

$$P_v \equiv \frac{I_v - I_h}{I_v + I_h} = 1 - \frac{2I_h}{I_v + I_h}. \quad (11)$$

Here, $I_h$ and $I_v$ are intensities of X-rays horizontally and vertically polarized. At angular positions (*b*) and (*c*) in Fig. 6 where $\Delta\theta_{PR_1} = -14.80, +14.08$ arcsec, $I_h/(I_v + I_h)$ had minimum values. At these angular positions, $P_v$ were estimated from (11) to be 0.943 and 0.935. These high values of $P_v$ were achieved by a large total thickness (7.941 mm) in addition to the effect of compensation for the off-axis and chromatic aberrations of the transmission-type X-ray phase retarders. In the experiment taking pinhole topographs with the incidence of vertical and $\pm 45^\circ$-inclined linearly polarized X-rays, $\Delta\theta_{PR_1}$ was adjusted at the angular position (*b*) in Fig. 6 keeping the condition of (9). At angular positions (*a*) and (*d*) in Fig. 6 where $\Delta\theta_{PR_1} = -27.52, +27.08$ arcsec, the values of $P_v$ were zero. Pinhole topographs with the incidence of right- and left-screwed circular polarization were taken by adjusting $\Delta\theta_{PR_1}$ at (*a*) and (*d*) in Fig. 6 keeping the condition of (9). The phase-retarder system can also generate horizontally polarized X-rays without removing the phase retarders from the X-ray path since $\Delta\phi_{\mathrm{total}}$ can be controlled to be zero by $\Delta\theta_{PR_n}$ whose signs are the same for $n \in \{1, 2, 3, 4\}$. When generating the horizontally polarized X-rays, $\Delta\theta_{PR_1}$ was adjusted to be 26.00 arcsec and $\Delta\theta_{PR_n}$ ($n \in \{2, 3, 4\}$) were set so that $\Delta\phi_{\mathrm{total}}$ given by (10) was zero, where the condition of (9) is approximately satisfied. The conditions for generating horizontal, vertical and $\pm 45^\circ$-inclined linear polarizations and right- and left-screwed circular polarizations are summarized in Table 3.

### 4.2. Sample crystal

Fig. 7 shows the experimental arrangement around the sample crystal. The sample was an undoped floating-zone silicon crystal with high resistivity (>2000 Ω cm). The dimensions of the sample crystal were 26, 29 and 9.60 mm in the

**Table 3**
$\chi_{PR}$ and $\Delta\theta_{PR_n}$ ($n \in \{1, 2, 3, 4\}$) are summarized for generating horizontal (LH), vertical (LV), right-screwed circular (RC), left-screwed circular (LC), $-45^\circ$-inclined linear (L − 45°) and $+45^\circ$-inclined linear (L + 45°) polarizations with which the experimental pinhole topographs were taken.

When $\Delta\theta_{PR_n}$ is positive, the *n*-numbered-quadrant phase retarder is angularly deviated from the Bragg angle to the high-angle side by $\Delta\theta_{PR_n}$. When $\chi_{PR} = 0$, the planes of incidence of the first-, second-, third- and fourth-quadrant phase retarders are inclined by 45, 135, 225 and 315°, respectively. $\chi_{PR}$ is positive when the $\chi_{PR}$ axis is rotated counterclockwise viewed from the downstream direction. L + 45° means that the plane of linear polarization is inclined by 45° counterclockwise viewed from the downstream direction.

| Incident polarization | $\chi_{PR}$ (°) | $\Delta\theta_{PR_1}$ (arcsec) | $\Delta\theta_{PR_2}$ (arcsec) | $\Delta\theta_{PR_3}$ (arcsec) | $\Delta\theta_{PR_4}$ (arcsec) |
|---|---|---|---|---|---|
| LH | 0 | −26.00 | −31.00 | −26.16 | −33.92 |
| LV | 0 | −14.80 | 17.64 | −14.88 | 19.32 |
| CR | 0 | −27.52 | 32.80 | −27.68 | 35.92 |
| CL | 0 | 27.08 | −32.28 | 27.24 | −35.32 |
| L − 45° | 22.5 | −14.80 | 17.64 | −14.88 | 19.32 |
| L + 45° | −22.5 | −14.80 | 17.64 | −14.88 | 19.32 |

directions [011], [21$\bar{1}$] and [1$\bar{1}$1]. The surfaces were chemically etched. A two-axis ($\omega$–$\phi$) swivel-type goniometer on which the sample was set was mounted on a $\chi$–$\theta$ goniometer so that the directions [011], [21$\bar{1}$] and [1$\bar{1}$1] of the crystal were approximately parallel to the $\phi$, $\theta$ and $\omega$ axes. The rotation angle around the $\chi$ axis, which was parallel to the direction of X-ray transmission, was adjusted so that the [21$\bar{1}$] direction of the sample was vertical in Fig. 7. The beam dimension was adjusted to be 100 × 100 μm. Before the imaging plate was set, 000-forward-diffracted (hereafter referred to as FD), 440- and 484-transmitted reflected (hereafter referred to as TR)

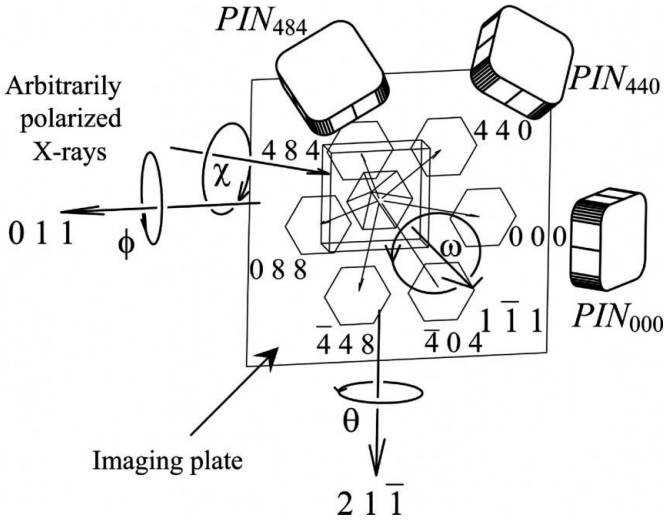


**Figure 7**
Experimental arrangement around a floating-zone silicon sample crystal with a thickness of 9.6 mm. A monochromated X-ray beam whose polarization state was controlled with the phase-retarder system shown in Fig. 3 was incident on the sample crystal. Six images of 000- (forward-diffracted) 440-, 484-, 088-, $\bar{4}48$- and $\bar{4}04$-transmitted-reflected X-rays were recorded simultaneously on an imaging plate placed 21 mm behind the sample crystal so that the surfaces of the sample and the imaging plate were parallel.

X-rays were searched with PIN photodiodes $PIN_{000}$, $PIN_{440}$ and $PIN_{484}$ in Fig. 7. Then $\theta$ and $\phi$ axes were adjusted so that FD and 440-TR and 484-TR X-rays were simultaneously strong at an angular position where the six-beam condition was satisfied. After that, the dimension of the incident X-ray beam was adjusted to be 25 × 25 μm with the slit *S* shown in Fig. 3. Then an imaging plate with a pixel size of 50 × 50 μm was placed 21 mm behind the exit surface of the sample crystal so that the $[1\bar{1}1]$ surface of the sample and the surface of the imaging plate were parallel. FD, 440-, 484-, 088-, $\bar{4}48$- and $\bar{4}04$-TR X-ray images were simultaneously recorded on the imaging plate.

## 5. Results and discussion

The experimentally obtained and computer-simulated pinhole topographs are shown in Figs. 8 and 9 with incident horizontal-linear and vertical-linear polarizations, respectively. Exposure time for Figs. 8(*a*) and 9(*a*) was 900 s.

Hereafter, the discussion is given with enlarged figures for each reflection index. Figs. 10, 11, 12 and 13 show experimental and computer-simulated topograph images of FD, 440-, 484- and 088-TR X-rays, respectively. (*a*), (*b*), (*c*) and (*d*) of Figs. 10–13 correspond to the incidence of horizontal-linearly, vertical-linearly, +45°-inclined linearly and right-screwed circularly polarized X-rays generated with the phase-retarder system. The exposure time was 300 s for [*E*(*a*)], [*E*(*b*)] and [*E*(*c*)], 900 s for [*E*(*d*)]. Both the experimental and computer-simulated images with incident −45°-inclined linearly polarized X-rays were symmetrical with respect to the horizontal center line to those with the incidence of +45°-inclined linearly polarized X-rays. Those with incident right- and left-screwed circularly polarized X-rays were identical.

Fig. 14(*a*) is an experimental FD topograph identical with Fig. 10[*E*(*d*)], which was obtained with an incidence of right-screwed circular polarization. The spot indicated by *S*(000) is a halation of the directly transmitted beam. Lines like knife edges indicated by *L*(440), *L*(484), *L*(088), *L*($\bar{4}48$) and *L*($\bar{4}04$)

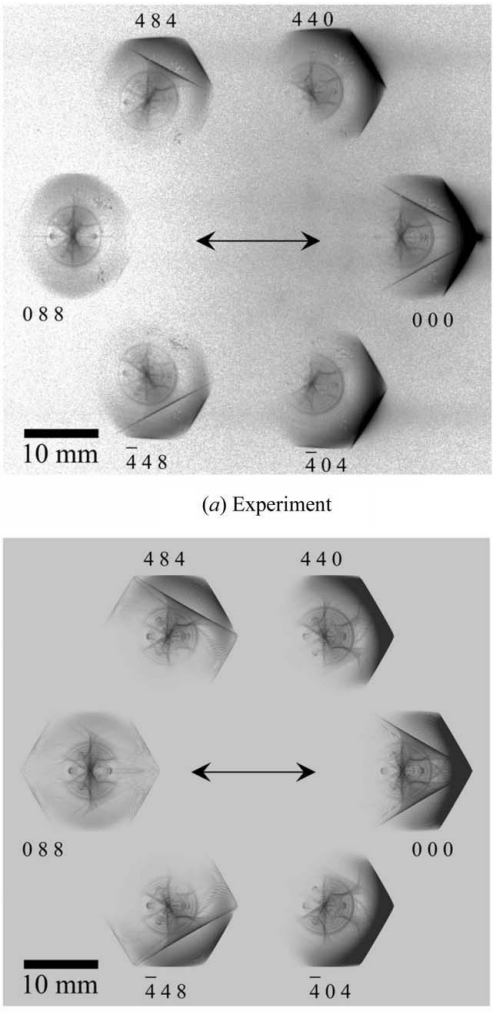


(*a*) Experiment




(*b*) Simulation

**Figure 8**
(*a*) Experimentally obtained and (*b*) computer-simulated pinhole topograph images with incident horizontally polarized X-rays.

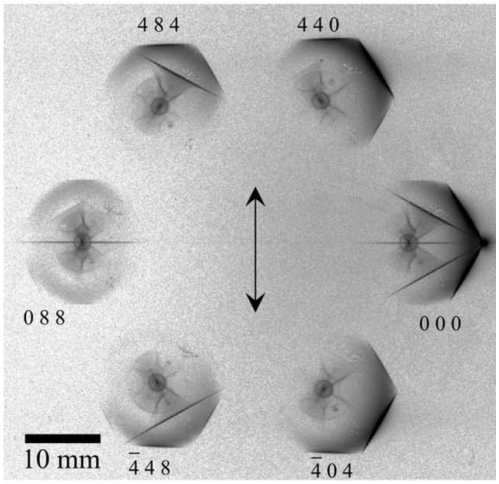


(*a*) Experiment

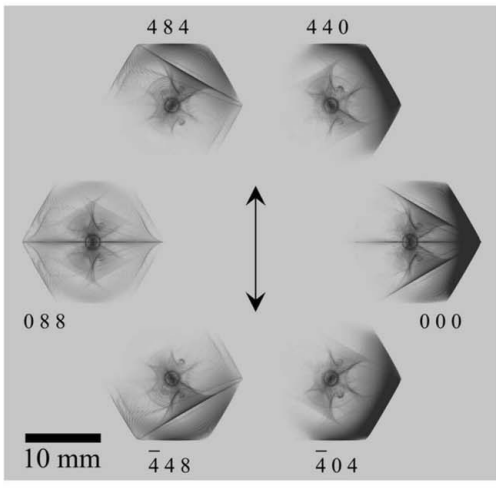


(*b*) Simulation

**Figure 9**
(*a*) Experimentally obtained and (*b*) computer-simulated pinhole topograph images with incident vertically polarized X-rays.

are parallel to the scattering vector of each reflection index. These lines are considered to be caused by a two-beam dynamical effect between the FD beam and one of the TR beams of each reflection index. In the cases of incident polarization where $L(hkl)$ exists in Fig. 10, knife-edge lines parallel to $L(hkl)$ are also observed in Figs. 8, 9, 11, 12, 13. In Figs. 10[$E(a)$] and 10[$S(a)$], $L(088)$ cannot be observed. Also, in Figs. 13[$E(a)$] and 13[$S(a)$], such knife-edge lines cannot be observed. The Bragg angle of the 088 reflection is 45.0548° as shown in Table 1. Then the polarization factor of the $\pi$ polarization in FD and the 088-TR two-beam case is a small value [$-1.91 \times 10^{-3} = \cos(2 \times 45.0548^\circ)$]. For this reason, the effect of direct energy transfer between FD and 088-TR beams is considered to be small. In Figs. 10[$E(c)$] and 10[$S(c)$], $L(\bar{4}48)$ cannot be observed, which can be explained by the same reason.

Large and small circular patterns indicated by $C_1$ and $C_2$ can be observed in Fig. 14($a$) {Fig. 10[$E(d)$]}. $C_2$ cannot be

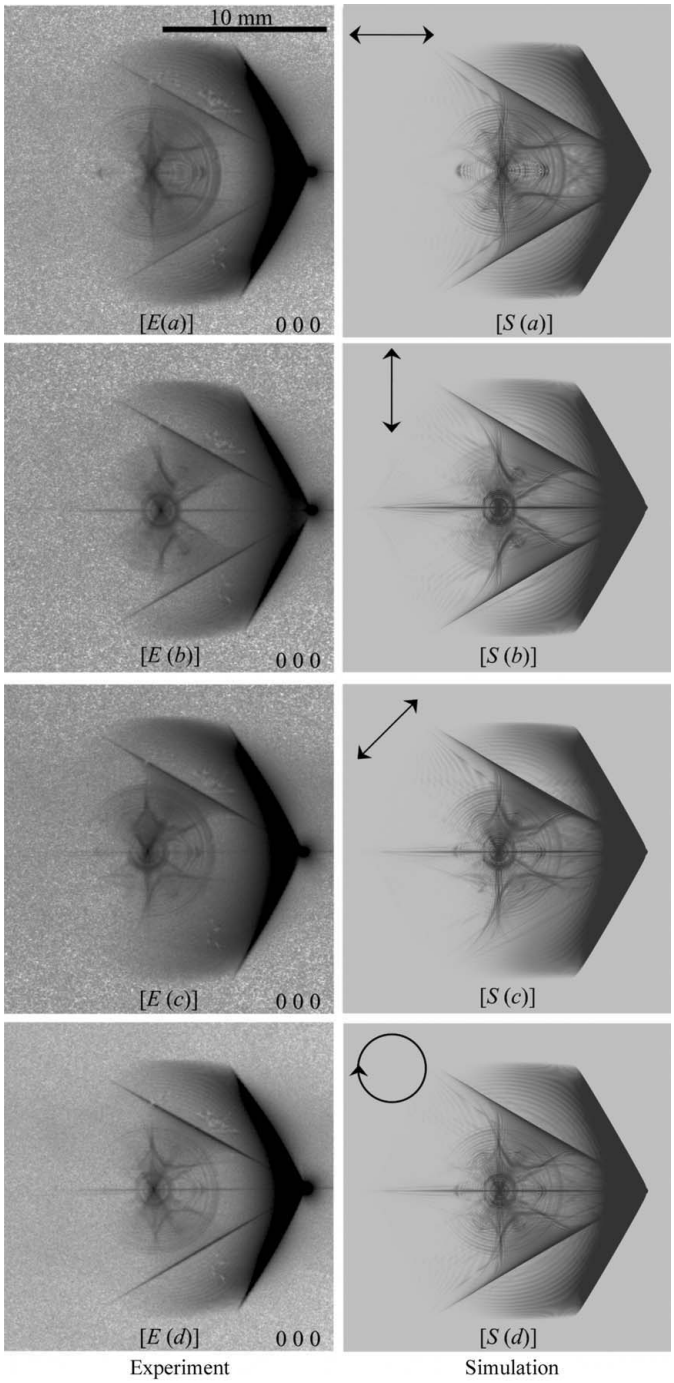


**Figure 10**
Experimentally obtained and computer-simulated pinhole topograph images of forward-diffracted (FD) X-rays.

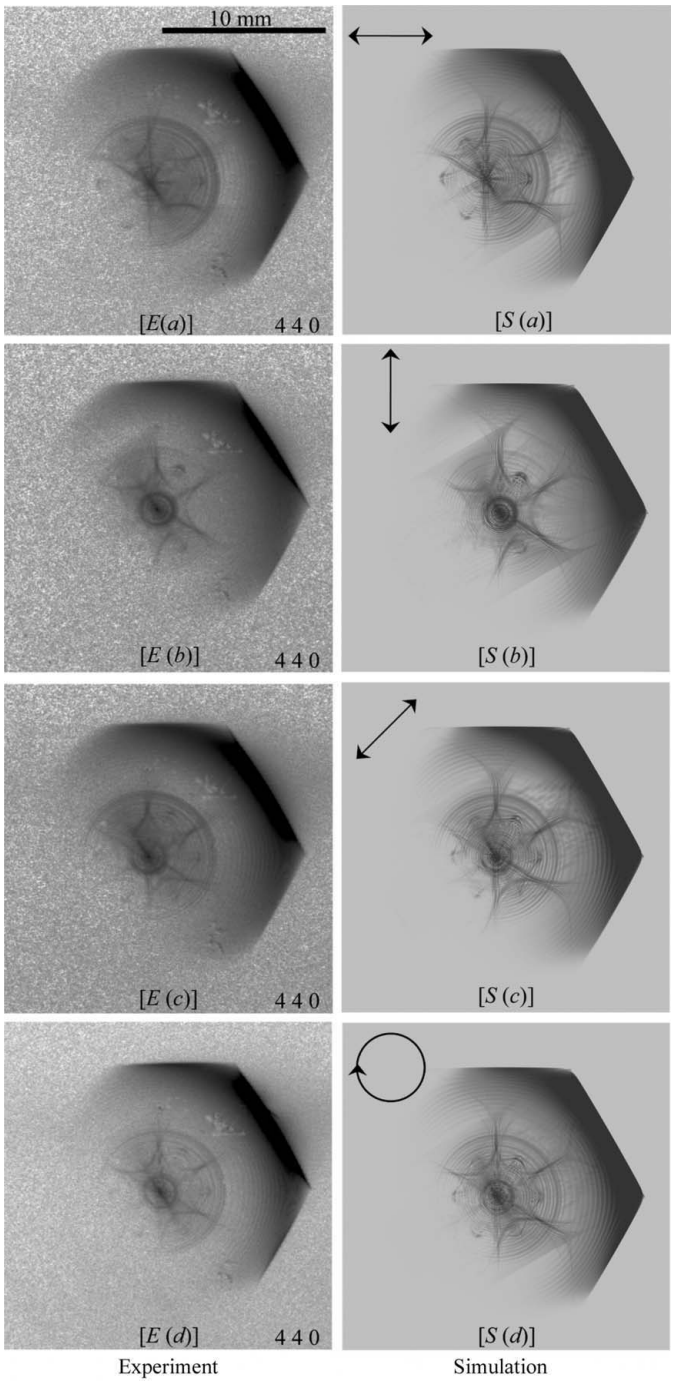


**Figure 11**
Experimentally obtained and computer-simulated pinhole topograph images of transmitted-reflected (TR) X-rays with the 440 reflection.

observed in [$E(a)$] and [$S(a)$] of Figs. 10–13. $C_1$ cannot be observed so clearly in [$E(b)$] and [$S(b)$] of Figs. 10–13. Therefore, it can be considered that $C_1$ and $C_2$ reveal the existence of a cone-shaped energy flow path caused by horizontally and vertically polarized components of the incident X-rays, respectively.

Three groups of white spots indicated by $S_1$, $S_2$ and $S_3$ can be observed in Fig. 14($a$). These are considered to be images of some defects on the exit surface of the sample since these images can be observed at the same position in all experimental topographs in Figs. 10–13.

Fig. 14($b$) shows cross-section gray-level profiles along the white line in Fig. 14($a$) for the experimental (left) and computer-simulated (right) topographs. The deepest gray (black) corresponds to a gray level of 256. A quantitative agreement is found between the experimental and computer-simulated profiles. Several characteristic patterns and regions can be observed. BGR are background regions outside the

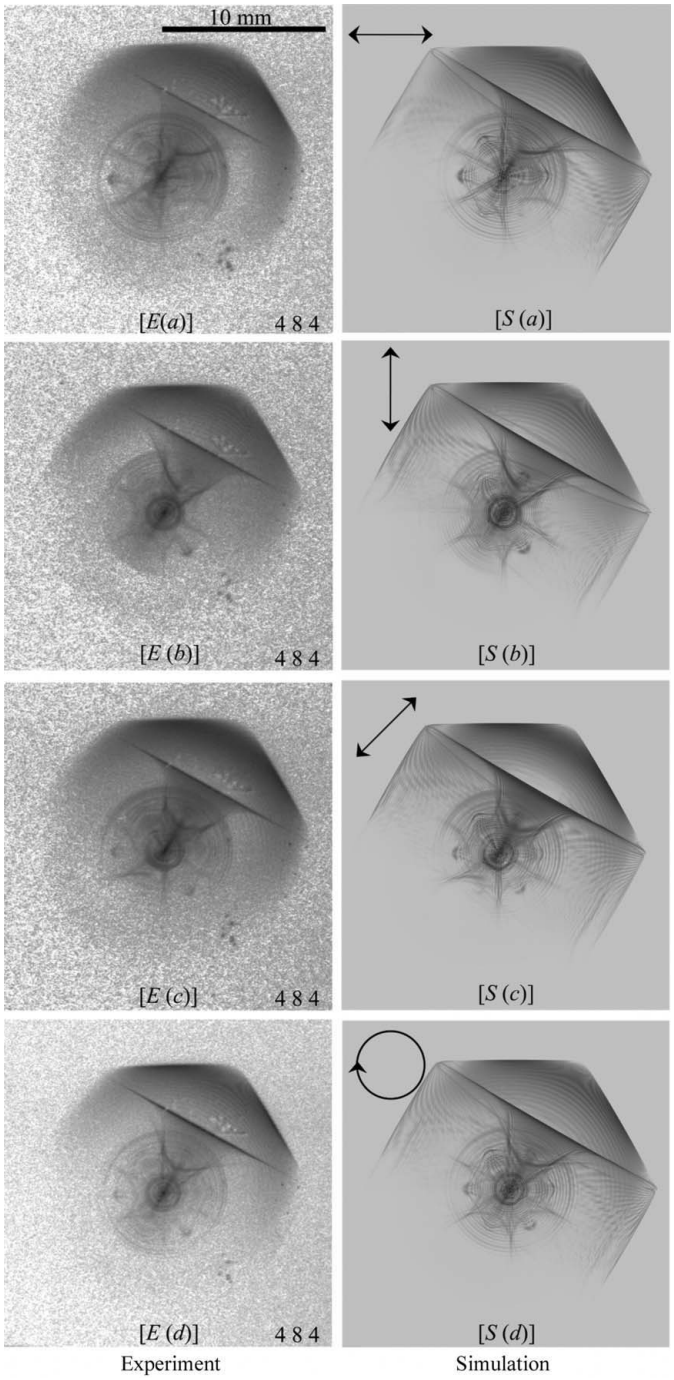


**Figure 12**
Experimentally obtained and computer-simulated pinhole topograph images of transmitted-reflected (TR) X-rays with the 484 reflection.

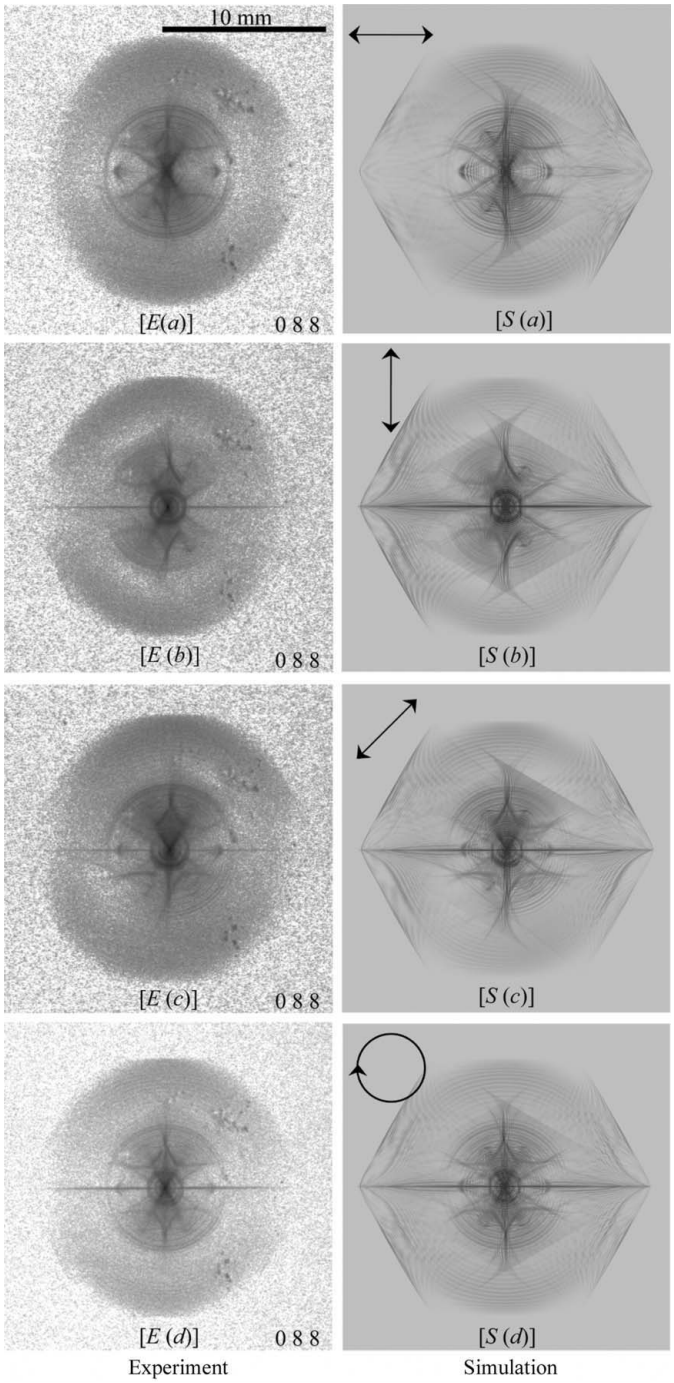


**Figure 13**
Experimentally obtained and computer-simulated pinhole topograph images of transmitted-reflected (TR) X-rays with the 088 reflection.

topograph image caused by X-rays scattered by air. FFR are fine fringe regions which can be found in all the experimental and computer-simulated topographs in Figs. 10–13. The features of FFR do not depend so strongly on the polarization state of the incident X-rays. $L(484)$ and $L(\bar{4}48)$ in Fig. 14($b$) correspond to the knife-edge lines observed in Fig. 14($a$). $C_1$ is the circular pattern considered to be mainly caused by the horizontally polarized component of the incident X-rays. $L(088)$ can be found at the central position of the profiles.

Incidentally, it should be noted that evident differences between Figs. 10[$E(c)$] and 10[$E(d)$] and between Figs. 10[$S(c)$] and 10[$S(d)$] can be observed. For the cases of ($c$) and ($d$), intensity ratios between horizontally and vertically polarized components of the incident X-rays are identical. Only phase-shift values are different. This reveals that the wavefields excited by the horizontally and vertically polarized incident X-rays interfere with each other.

## 6. Conclusions

The Takagi–Taupin X-ray $n$-beam dynamical theory and the computer algorithm to solve the theory has been almost completely verified from comparison between experimental and computer-simulated six-beam pinhole topographs. It was revealed that the Takagi–Taupin $n$-beam theory can deal with the effect of polarization correctly from the strong dependence on incident polarization on both experimental and computer-simulated pinhole topograph images. The efficiency of the rotating four-quadrant phase-retarder system designed to generate arbitrarily polarized X-rays was also confirmed at a photon energy as high as 18.245 keV.

The part of theory and computer simulation of the present work was performed at the High-Power X-ray Laboratory, Nano-Engineering Research Center, Institute of Engineering Innovation, Graduate School of Engineering, The University of Tokyo. The preliminary experiments were performed at AR-BL03A of the Photon Factory AR under the approval of the Photon Factory Program Advisory Committee (Proposals No. 2003 G202 and No. 2003 G203). The main experiment was performed at BL09XU of SPring-8 under the approval of Japan Synchrotron Radiation Research Institute (JASRI) (Proposals No. 2002 A0499-NMD3-np, No. 2003B0594-NM-np and No. 2004 A0330-ND3c-np). The present work is one of the activities of the Active Nano-Characterization and Technology Project financially supported by Special Coordination Fund of the Ministry of Education, Culture, Sports, Science and Technology of the Japan government. The authors are indebted to Professor Emeritus S. Kikuta and Professor Y. Amemiya of The University of Tokyo for their encouragement of the present study and are also indebted to Dr T. Oguchi of the SPring-8 Service Company for his excellent technical assistance in the experiment.

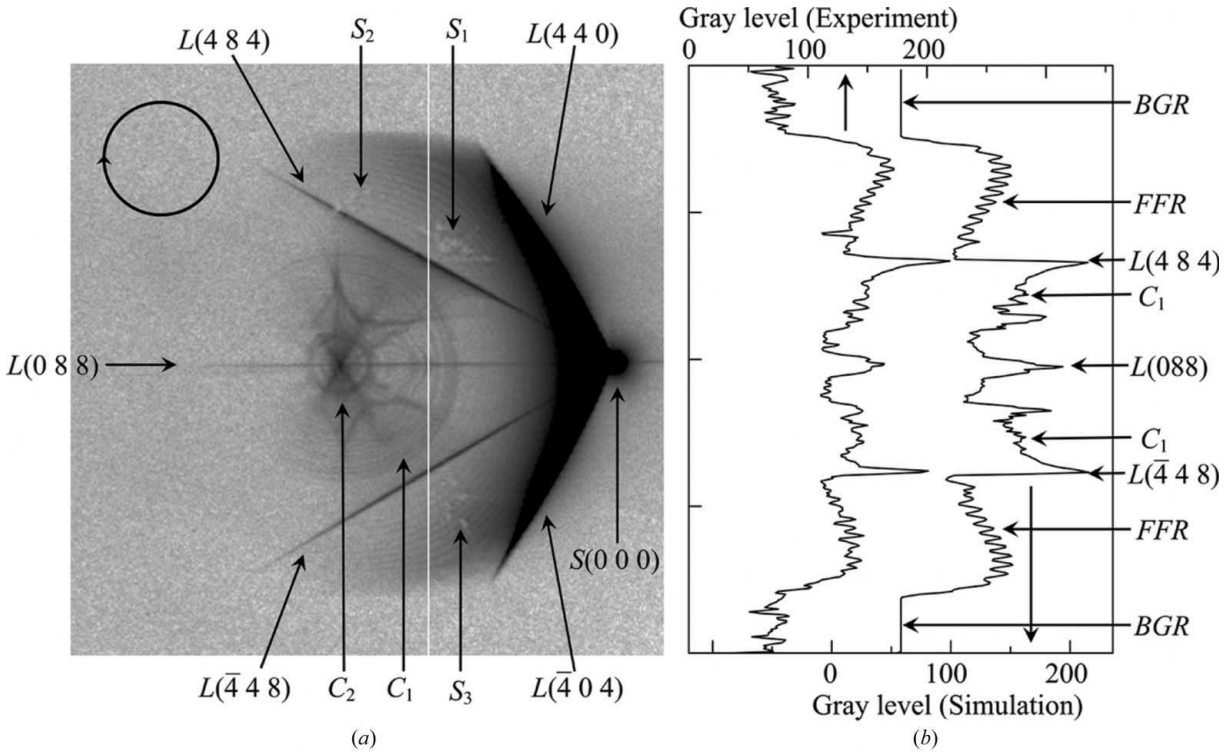


**Figure 14**
($a$) This topograph is the same as Fig. 10[$E(d)$], which was an experimentally obtained forward-diffracted (FD) image with the incidence of X-rays with right-screwed circular polarization. ($b$) Cross-section gray-level profiles on the white line drawn in ($a$) for the experimental (left) and computer-simulated (right) topograph images. The darkest gray (black) corresponds to a gray level of 256.

## References


Authier, A. (2005). *Dynamical Theory of X-ray Diffraction*, reprinted with revisions 2004, 2005. Oxford University Press.

Chang, S.-L. (1998). *Acta Cryst.* A**54**, 886–894.

Chang, S.-L. (2004). *X-ray Multiple-Wave Diffraction, Theory and Application.* Berlin: Springer.

Colella, R. (1974). *Acta Cryst.* A**30**, 413–423.

Colella, R. (1995*a*). *Comm. Condens. Matter Phys.* **17**, 175–198.

Colella, R. (1995*b*). *Comm. Condens. Matter Phys.* **17**, 199–215.

Darwin, C. G. (1914*a*). *Philos. Mag.* **27**, 315–333.

Darwin, C. G. (1914*b*). *Philos. Mag.* **27**, 675–690.

Ewald, P. P. (1917). *Ann. Phys. 4. Folge*, **54**, 519–597.

Ewald, P. P. & Héno, Y. (1968). *Acta Cryst.* A**24**, 5–15.

Giles, C., Malgrange, C., Goulon, J., de Bergevin, F., Vettier, C., Dartyge, E., Fontaine, A., Giorgetti, C. & Pizzini, S. (1994). *J. Appl. Cryst.* **27**, 232–240.

Giles, C., Malgrange, C., Goulon, J., de Bergevin, F., Vettier, C., Fontaine, A., Dartyge, E. & Pizzini, S. (1994). *Nucl. Instrum. Methods A*, **349**, 622–625.

Hart, M. & Rodrigues, A. R. D. (1979). *Philos. Mag. B*, **40**, 149–157.

Härtwig, J. (1987). *Acta Cryst.* A**43**, 522–525.

Héno, Y. & Ewald, P. P. (1968). *Acta Cryst.* A**24**, 16–42.

Heyroth, F., Zellner, J., Höche, H.-R., Eisenschmidt, C., Weckert, E. & Drakopoulous, M. (2001). *J. Phys. D: Appl. Phys.* **34**, A151–A157.

Hildebrandt, G. (1967). *Phys. Status Solidi*, **24**, 245–261.

Hirano, K., Ishikawa, T. & Kikuta, S. (1993). *Nucl. Instrum. Methods Phys. Res. A*, **336**, 343–353.

Hirano, K., Ishikawa, T. & Kikuta, S. (1995). *Rev. Sci. Instrum.* **66**, 1604–1609.

Hirano, K., Ishikawa, T., Koreeda, S., Fuchigami, K., Kanzaki, K. & Kikuta, S. (1992). *Jpn. J. Appl. Phys.* **31**, L1209–L1211.

Hirano, K., Izumi, K., Ishikawa, T., Annaka, S. & Kikuta, S. (1991). *Jpn. J. Appl. Phys.* **30**, L407–L410.

Larsen, H. B. & Thorkildsen, G. (1998). *Acta Cryst.* A**54**, 129–136.

Laue, M. von (1931). *Ergeb. Exakten Naturwiss*. **10**, 133–158.

Okitsu, K. (2003). *Acta Cryst.* A**59**, 235–244.

Okitsu, K., Imai, Y., Ueji, Y. & Yoda, Y. (2003). *Acta Cryst.* A**59**, 311–316.

Okitsu, K., Ueji, Y., Sato, K. & Amemiya, Y. (2002). *Acta Cryst.* A**58**, 146–154.

Renninger, M. (1937). *Z. Phys.* **106**, 141–176.

Suzuki, M., Kawamura, N., Mizumaki, M., Urata, A., Maruyama, H., Goto, S. & Ishikawa, T. (1998). *Jpn. J. Appl. Phys.* **37**, L1488–L1490.

Takagi, S. (1962). *Acta Cryst.* **15**, 1311–1312.

Takagi, S. (1969). *J. Phys. Soc. Jpn*, **26**, 1239–1253.

Taupin, D. (1964). *Bull. Soc. Fr. Minéral. Cristallogr.* **87**, 469–511.

Thorkildsen, G. (1987). *Acta Cryst.* A**43**, 361–369.

Thorkildsen, G. & Larsen, H. B. (1998). *Acta Cryst.* A**54**, 120–128.

Weckert, E. & Hümmer, K. (1997). *Acta Cryst.* A**53**, 108–143.

Weckert, E. & Hümmer, K. (1998). *Cryst. Res. Technol.* **33**, 653–678.